CHEMISTRY
A EUROPEAN JOURNAL

DOI: 10.1002/chem.200901688

Investigation of the Mechanism of Colloidal Silicalite-1 Crystallization by Using DLS, SAXS, and ^{29}Si NMR Spectroscopy**

Alexander Aerts,*[a] Mohamed Haouas,[b] Tom P. Caremans,[a] Lana R. A. Follens,[a] Titus S. van Erp,[a] Francis Taulelle,[b] Jan Vermant,[c] Johan A. Martens,*[a] and Christine E. A. Kirschhock[a]

Abstract: Colloidal silicalite-1 zeolite was crystallized from a concentrated clear sol prepared from tetraethylorthosilicate (TEOS) and aqueous tetrapropylammonium hydroxide (TPAOH) solution at 95 °C. The silicate speciation was monitored by using dynamic light scattering (DLS), synchrotron small-angle X-ray scattering (SAXS), and quantitative liquid-state ^{29}Si NMR spectroscopy. The silicon atoms were present in dissolved oligomers, two discrete nanoparticle populations approximately 2 and 6 nm in size, and crystals. On the basis of new insight into the evolution of the different nanoparticle populations and of the silicate connectivity in the nanoparticles, a refined crystallization mechanism was derived. Upon combining the reagents, different types of nanoparticles (ca. 2 nm) are formed. A fraction of these nanoparticles with the least condensed silicate structure does not participate in the crystallization process. After completion of the crystallization, they represent the residual silicon atoms. Nanoparticles with a more condensed silicate network grow until approximately 6 nm and evolve into building blocks for nucleation and growth of the silicalite-1 crystals. The silicate network connectivity of nanoparticles suitable for nucleation and growth increasingly resembles that of the final zeolite. This new insight into the two classes of nanoparticles will be useful to tune the syntheses of silicalite-1 for maximum yield.

Keywords: nanoparticles · NMR spectroscopy · SAXS · silicalites · zeolites

Introduction

The synthesis of colloidal silicalite-1 from an optically clear sol, introduced some 15 years ago by Persson et al.,[1] is a convenient system for the experimental investigation of zeolite crystallization. The starting mixture is obtained by hydrolysis of tetraethylorthosilicate (TEOS) in aqueous tetrapropylammonium hydroxide (TPAOH). Silica is mainly present as nanoparticles 2–10 nm in size, depending on the exact procedure. The initial mixture is transparent and usually termed a clear solution, although a clear sol would be a better designation considering the presence of colloidal nanoparticles. The formation of silicalite-1 is extremely slow at ambient temperature and takes months to years.[2–4] By heating a clear sol, for example, at 90 °C, the crystallization time of colloidal silicalite-1 is shortened to about one day.

Because of their small size and strong sensitivity to changes in the solution, characterization of the nanoparticles and identification of their role in the crystallization of silicalite-1 is challenging. Scattering techniques carried out in situ, such as dynamic light scattering (DLS) and synchrotron small-angle X-ray scattering (SAXS), have been successfully applied to determine the particle dimensions and shapes.[5–8] The silicon speciation is accessible through liquid-state ^{29}Si NMR spectroscopy.[5,6,9] Cryo-TEM analysis of frozen clear sols and TEM analysis of dried sols revealed the presence of a zeolite lattice in small particles collected early in the crys-

[a] Dr. A. Aerts, T. P. Caremans, Dr. L. R. A. Follens, Dr. T. S. v. Erp, Prof. J. A. Martens, Prof. C. E. A. Kirschhock
Centre for Surface Chemistry and Catalysis
K.U. Leuven, Kasteelpark Arenberg 23
3001 Heverlee (Belgium)
Fax: (+32) 16-32-19-98
E-mail: johan.martens@biw.kuleuven.be

[b] Dr. M. Haouas, Dr. F. Taulelle
Institut Lavoisier de Versailles
Université de Versailles St. Quentin en Yvelines
45 avenue des Etats-Unis, 78035 Versailles (France)

[c] Prof. J. Vermant
Department of Chemical Engineering
K.U. Leuven, Willem de Croylaan 46
3001 Heverlee (Belgium)

[**] DLS = dynamic light scattering SAXS = small-angle X-ray scattering.

Supporting information for this article is available on the WWW under http://dx.doi.org/10.1002/chem.200901688.

tallization process.[3,10–12] Nanoslab-shaped nanoparticles have been observed after spreading the clear sol on a TEM grid.[4]

Based on the variety of experimental approaches and investigations of clear sols, several models for the crystallization of silicalite-1 have been proposed. The rival models differ in the nature of the silicate species responsible for crystal growth, the extent of zeolitic order within the nanoparticles, and the involvement of aggregation steps.

Some authors proposed growth of silicalite-1 crystals from the silicate monomer, either all through the process[13] or after an aggregation phase to reach a critical size.[14] Other authors invoked the monomer-addition mode to explain the last stage of the crystallization process and the development of crystal facets in a crystal-ripening phase.[10] In an early model by Burkett and Davis for the crystallization of ZSM-5, the Al-containing counterpart of silicalite-1, particles 2.8 nm in size containing tetrapropylammonium (TPA) ions, form aggregates of 5–10 nm.[15] Dokter et al. proposed a similar scheme, with an aggregation of primary units into aggregates 5–10 nm in size.[16] Through internal structuring, these aggregates become viable crystal nuclei. In a subsequent step, still larger aggregates are formed, which densify and restructure to become final crystals. In the model by de Moor et al., a prenucleation step that involves aggregation of elementary particles and subsequent internal restructuring of the aggregate to form a nucleus were adopted (Figure 1 a).[17] Crystal growth was proposed to occur by addition of elementary particles to nuclei. After the addition, an internal rearrangement of attached nanoparticles is required to become part of the crystal lattice (Figure 1 a). Nikolakis et al. adhered to a similar crystal-growth model that involves the addition of nanoparticles.[18]

Several authors monitored formation of silicalite-1 from a clear sol at room temperature over a period of months to years.[2–4] Almost single-crystalline, composite crystals with domain sizes of approximately 6 nm were observed with TEM analysis,[3,4,10,11] thus hinting at aggregative growth from such prestructured units. Davis et al. built a kinetic model for this type of oriented aggregative growth (Figure 1 b).[3] Nanoparticles have been proposed to adopt a range of internal structures during prenucleation, from structureless to zeolite-like, the latter feeding nucleation and aggregative crystal-growth processes. Internal structuring of the particles was proposed to be a time-consuming process.

An early aggregative growth model in which the silicalite-1 framework connectivity is present at all stages of the aggregation process was proposed by Kirschhock et al. (Figure 1 c).[19,20] Precursor species with 33–36 silicon atoms that hold one TPA unit in a channel intersection were proposed to aggregate into nanoslabs, then into tablets, and staples of tablets that assemble into final crystals.

Evidence for aggregative steps in the formation of silicalite-1 is accumulating and was found in crystallizations from both concentrated[4,10,19,20] (H_2O/TEOS = 15–20:1) and dilute[3] (H_2O/TEOS > 238:1) sols. Some critical issues remain unanswered. The key questions are: the stage at which nanoparticles are structured and whether individual particles and aggregates can undergo internal structuring. The observation of X-ray diffraction in situ and observation of electron diffraction ex situ are obvious tools for detecting structuring of particles that present several unit cells. In smaller particles, such as the ones observed in clear sols, one must rely on molecular tools, such as ^{29}Si NMR or IR spectroscopy.[21] Rimer et al. developed an indirect method to probe the molecular structure of nanoparticles by measuring dissolution enthalpies and rates.[22]

The gathered evidence shows that the crystallization of silicalite-1 cannot be described entirely by classical nucleation and growth theories. In addition to the classical concept of critical nucleus size, the phenomenon of zeolite-framework development must be taken into ac-

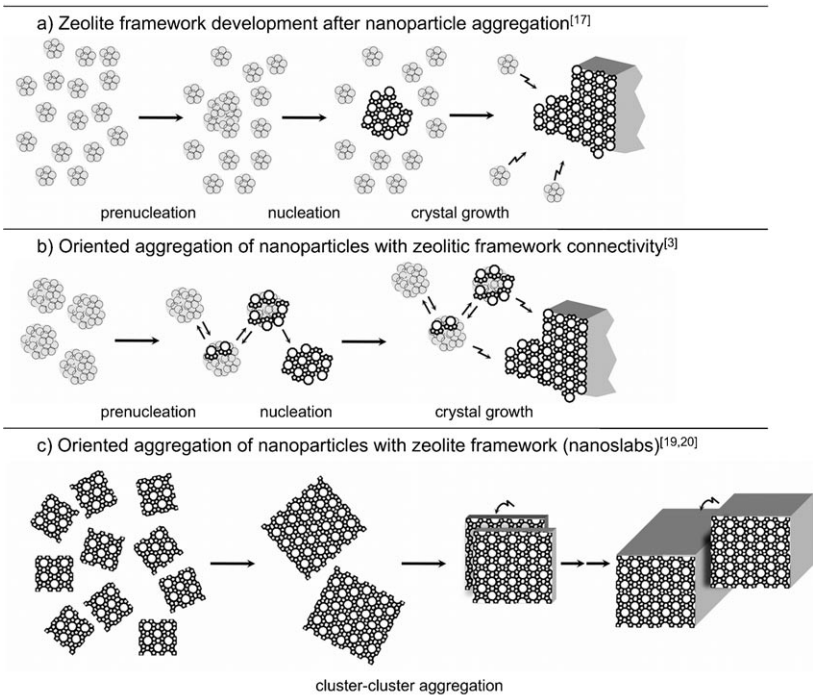

Figure 1. An overview of aggregative crystallization mechanisms proposed previously. Particles with poorly developed framework connectivity are depicted in light gray; zones with zeolitic framework connectivity are depicted in dark gray; the zigzag arrows indicate an aggregation event.

count. In the model given in Figure 1a, the formation of a nucleus occurs in two steps, that is, growth by nanoparticle aggregation followed by zeolite-framework development. In the model given in Figure 1b, the nucleus is defined in terms of the extent of the zeolite-framework development only. Because of the development of the framework, the formation and dissociation of the nucleus is not completely reversible as it is in the "classical" case. In the remainder of this report, we adhere to the term "nucleus" to define those particles from which one crystal starts growing in the initial stages. Herein, the concept of the nucleus is hence defined in a broader sense, irrespective of mechanistic details.

Thus far, ^{29}Si NMR spectroscopy has been applied to the starting clear sol and in the first period of heating before the emergence of the first crystals.[5,6,9] Herein, we extend the investigation over the entire crystallization process and combine ^{29}Si NMR spectroscopy with DLS and synchrotron SAXS to seek answers to the standing questions. Gaining insight into the structuring of nanoparticles involved in zeolite crystallization not only is of fundamental importance, but also has immediate practical impact. This insight will help to guide syntheses to better structured materials, higher product yields, and larger throughput.

Results

DLS: The clear sol was prepared from TEOS, TPAOH, and water and aged at ambient temperature for 24 h. A sample of the sol was taken and measured with DLS and viscometry at 25 °C. The sol viscosity was 6.7 mPa s. This sample is referred to as having a heating time of zero. Another small sample was introduced in the DLS instrument and heated at 95 °C to provoke crystallization of silicalite-1. In parallel, a third sample was heated at 95 °C in the measuring capillary of a viscosimeter, and the viscosity was measured (see Figure S1 in the Supporting Information). After heating for 12 h, multiple scattering occurred due to extensive crystal formation. Samples at heating times of more than 12 h were obtained by heating the clear sol at 95 °C in a synthesis oven, and quenching the samples to room temperature after selected heating times up to 32 h. To suppress multiple scattering, these samples were diluted 100-fold with water (v/v) before DLS and viscosity measurements at 25 °C. The viscosity of the samples after dilution was equal to that of water.

Intensity-weighed particle-diameter distributions were obtained from the DLS data through inverse Laplace transformation of the measured autocorrelation functions, viscosities, and application of the Stokes–Einstein equation (see Figures S1–S3 in the Supporting Information). The evolution of the peak maxima of the particle-diameter distributions with time is presented in Figure 2. At time zero, a single population of nanoparticles with a diameter of approximately 2.4 nm was observed, in agreement with earlier studies.[5] Upon heating, the maximum in the size distribution shifted from 2.4 nm to approximately 6 nm. A second population of larger particles that measured over 20 nm emerged after heating for 5 h. In the following, we will use the term "crystals" to denote the large particles, thus realizing that they may not be fully crystalline initially. The size of the crystals increased almost linearly with time to about 100 nm (Figure 2). This final crystal size corresponded well with the crystal size obtained in similar experiments and determined with SEM analysis.[29] The continuous linear increase in the crystal diameters at around a heating time of 12 h shows that the influence of sample dilution and measurement temperature on crystal-size determination is negligible.

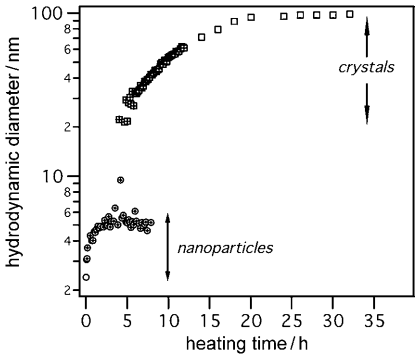

Figure 2. Hydrodynamic particle diameters determined with DLS analysis at various reaction times. Crossed symbols refer to measurements at the reaction temperature (95 °C); open symbols refer to measurements at 25 °C; open squares correspond to samples that were diluted with water before the DLS measurement.

For estimating the relative volume of each population, intensity-weighed particle-size distributions were converted into volume-weighed distributions. At the first observation of the silicalite-1 phase after 5 h, the relative volume of silicalite-1 crystals according to DLS was below 5 %. The scattering by silicalite-1 particles after 8 h already represented over 95 % of the total intensity. At later times, due to intense scattering by crystals, the nanoparticle population ceased to be detectable with DLS analysis.

SAXS: The SAXS patterns of sols at different stages of the crystallization were recorded at room temperature. The patterns of the unheated sol (heating time of 0 h) and of sols heated at 95 °C and subsequently quenched to room temperature after different heating times are shown in Figure 3.

The SAXS curve at a heating time of zero displayed a maximum value at a wave vector q of 1.8 nm^{-1}. The SAXS pattern after 4 h of heating displayed shoulders at around $q=1$ and 2.7 nm^{-1}, thus indicating that two subpopulations of nanoparticles of discrete size were present at this stage. The characteristic lengths $2\pi/q$ associated with the shoulders may be taken as an estimate of the average diameter of each subpopulation, that is, approximately 6 and 2 nm. A comparison of the sample heated for 4 h with a sample containing ten times more water confirmed that the shoulder at around $q=1$ nm^{-1} was caused by form factor scattering of nanoparticles and not by structure factor contributions

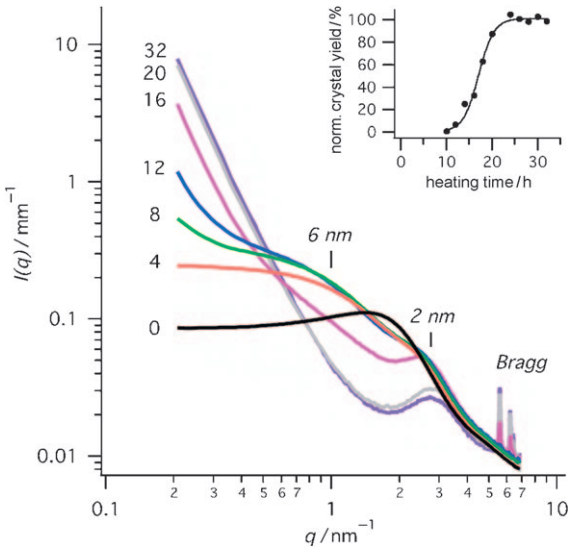

Figure 3. SAXS patterns measured at room temperature of samples quenched after various reaction times at 95 °C (reaction times in hours are shown next to the traces). Inset: crystal yield estimated from the area of MFI-type Bragg reflections normalized to the area after a heating time of 32 h.

caused by interparticle interactions (see Figure S4 in the Supporting Information). The shoulder at $q=2.7\ nm^{-1}$ evolves into a maximum at later heating times (>16 h), indication that the shoulder and the maximum are caused by the same population of nanoparticles. The maximum is characteristic for a structure factor contribution to the scattering pattern. The position of the shoulder and the maximum relates to the mean interparticle (center-to-center) spacing. Therefore, the value of approximately 2 nm estimated from the position of the shoulder is an upper limit for the diameter of the corresponding nanoparticle population.

The SAXS intensity at around $q=1\ nm^{-1}$ increased during heating for 0–4 h, thus suggesting a gradual formation of ≈6-nm nanoparticles. An additional SAXS pattern after heating for 2 h is shown in Figure S5 in the Supporting Information. The intensity above $q=2.7\ nm^{-1}$ remained constant between 0 and 4 h of heating, thus revealing that the size of the small nanoparticles (ca. 2 nm) did not change during formation of the 6-nm nanoparticles. Thus, SAXS and DLS analysis suggest that out of the initial particles with an average hydrodynamic diameter of 2.4 nm, a fraction grows to approximately 6 nm and another fraction remains at approximately 2 nm. DLS analysis fails to resolve these two populations because of their small size difference. The single nanoparticle diameter measured with DLS is the intensity-weighed average diameter of the populations that are approximately 2 and 6 nm.

It was derived from the SAXS pattern after 4 h that the scattering characteristic for 2- and 6-nm nanoparticles occurs in the region above $q=0.5\ nm^{-1}$ because crystals are not yet detected in the sol at this heating time with DLS analysis. Consequently, the increase in the scattering intensity at values below $q=0.5\ nm^{-1}$ at heating times of more than 4 h was ascribed to the formation and growth of silicalite-1 crystals (Figure 3).

When using DLS analysis, it was not possible to monitor the nanoparticles and the growing crystals simultaneously after heating for 8 h. When using SAXS, however, the nanoparticles and crystals can be observed in parallel during the whole crystallization process. During the period 5–12 h, SAXS analysis revealed that the size and number of both the 2 and 6-nm nanoparticles evolved only slightly, as evidenced by the small changes in the intensity and pattern shape at $q>0.5\ nm^{-1}$. The intensity of the shoulder at around $q=1\ nm^{-1}$ decreased after 16 h of heating, thus revealing a decrease in the number of the 6-nm nanoparticles, whereas the shoulder at $q=2.7\ nm^{-1}$ developed into a local maximum. SAXS analysis revealed, consistent with DLS analysis, that the crystals reached their final size after 20 h. The scattering of the final crystals showed power law decay and extended to the tail of low q values of the local maximum at $q=2.7\ nm^{-1}$. Thus, SAXS analysis revealed that the growth of crystals went along with depletion of the 6-nm nanoparticles during heating for 16–20 h, whereas the subpopulation of 2-nm nanoparticles remained present all through the crystallization process and persisted even after the end of crystal growth.

Bragg reflections were first detected after a reaction time of 10 h (Figure 3), at a crystal size of around 50 nm according to DLS analysis (Figure 2). The intensity of the MFI-type Bragg reflections provided a measure of the volume of silicalite-1 crystalline material. The crystallization yield according to SAXS analysis is presented in Figure 3. The SAXS and DLS analysis define the period of 0–5 h before the detection of crystals as the induction period. Nucleation and crystal growth proceeded during 5–20 h.

NMR spectroscopy: The ^{29}Si NMR spectra of sols at different stages of the crystallization were recorded at room temperature. Representative spectra of the unheated sol and sols heated at 95 °C and subsequently quenched to room temperature after different heating times (up to 35 h) are shown in Figure 4.

The ^{29}Si NMR spectrum of the unheated clear sol (Figure 4a) and after different heating times (Figure 4b) displayed narrow, liquidlike signals with a linewidth of approximately 1 Hz superimposed on broad signals with linewidths of 100–700 Hz. The narrow signals arose from dissolved oligomeric silicate species, and the broad signals from nanoparticles.[5] Individual signals can be assigned to Q^n environments. The spectral region of the Q^n environments is indicated in Figure 4b.

To verify if ageing at room temperature affected the silicate speciation in the clear sol, 12 ^{29}Si NMR spectra were recorded in the 24-hour period after the addition of water to the mixture of TEOS and aqueous TPAOH (40 wt %). The measurement time per spectrum was 2 h. No significant changes in peak intensity and chemical shift were observed,

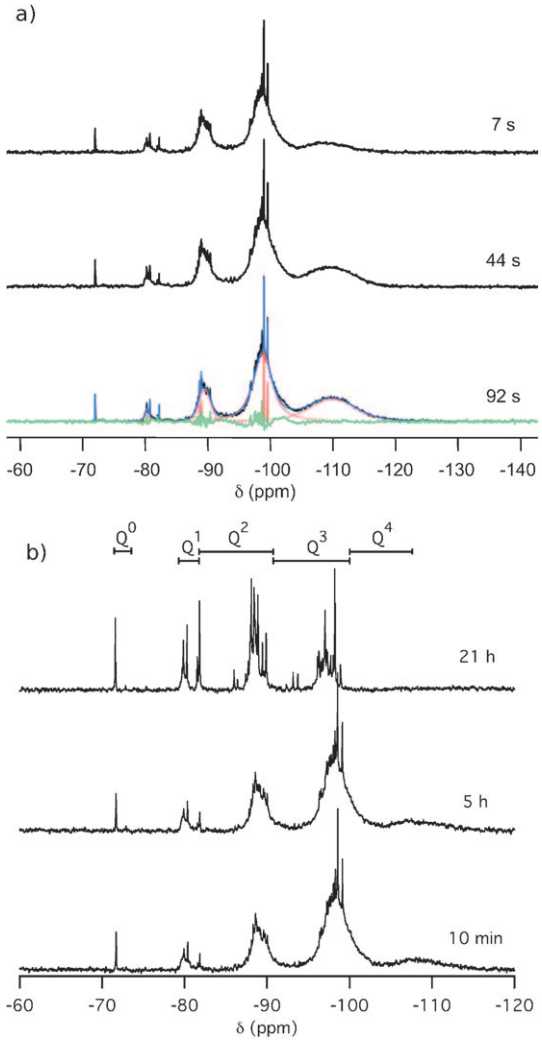

Figure 4. a) Liquid-state ^{29}Si NMR spectrum of the unheated clear sol collected by using different repetition delay times (t_d) of 7, 44, and 92 s. The fit to determine the contribution of nanoparticles and oligomers is shown for the spectrum for $t_d = 92$ s. b) Representative liquid-state ^{29}Si NMR spectra ($t_d = 7$ s) at different heating times indicated next to the traces.

thus showing that the silicate speciation did not evolve significantly.

The repetition delay time between radiofrequency pulses in the ^{29}Si NMR spectroscopic experiment needed to be long enough to ensure spin-lattice relaxation. In a previous ^{29}Si NMR spectroscopic investigation of a clear sol, a repetition delay of 7 s for a 45° pulse was used. Provis et al. pointed out that this timing resulted in partial relaxation of especially Q^4 silicon nuclei.[9] Those authors applied a repetition delay of 90 s. In the present study, ^{29}Si NMR spectroscopy was performed on the unheated clear sol by using either a delay time of 7 or 92 s, thus allowing complete spin-lattice relaxation for time constants T_1 smaller than 20 and 265 seconds, respectively. For comparison, Q^4 sites in TPA/silicalite-1 powder, the end-product of the synthesis, have a T_1 value of 145 seconds.[30] The use of a delay time of 92 seconds instead of 7 seconds (Figure 4a) resulted in an increase in the broad Q^3 signal of nanoparticles by a factor of 1.24 and Q^4 sites in nanoparticles by a factor of 3.30. For the Q^n signals of dissolved oligomers and the Q^1 and Q^2 signals of nanoparticles, both repetition times were adequate. The ^{29}Si NMR spectra of heated samples (Figure 4b) were recorded by using a delay time of 7 s instead of 92 s, which kept the experimentation time within reasonable limits to reach a sufficiently high signal-to-noise ratio necessary for accurate simulation, especially for the broad resonances. In the quantification, the Q^3 and Q^4 signal intensities of nanoparticles were corrected for incomplete T_1 relaxation by using the factors determined for the unheated sample. The correction was applied with the assumption that the spin-lattice relaxation time of the Q^3 and Q^4 signals of nanoparticles did not increase significantly during the course of the crystallization process.

The averaged total intensity of the spectra in the induction stage (0–5 h), corrected for partial relaxation, remained quasi constant and was considered as the total amount of silicon atoms present in the system. The DLS and SAXS analysis revealed that the content of crystals was negligible between 0 and 5 h. In the nucleation and crystal growth period (>5 h), the signal intensity decreased because of the formation of silicalite-1 crystals undetected by liquid-state NMR spectroscopy. The undetected fraction amounted to 64±5% of the total silicon content in the sample after 35 h of heating. This value agrees well with the yield of silicalite-1 recovered by centrifugation (60%), thus confirming that the undetected silicon fraction eventually represents the zeolite crystals. The crystals are not detected because of their large particle size, thus causing their rotational diffusion to be insufficiently rapid to average the anisotropy of solid-state nuclear interactions effectively and resulting in extremely broadened solid-state-like signals. Even the smallest crystals observed by DLS analysis (20–30 nm; see Figure 2) have a rotational correlation time, which scales with the particle volume, two orders of magnitude larger than the nanoparticles.

The large linewidth difference between the NMR signals for the oligomers and nanoparticles enabled decomposition of the spectrum and determination of the fraction of silicon atoms in the oligomers and nanoparticles (Figure 5) and the Q^n silicon connectivity distribution of the particles and oligomers separately (Figures 7 and 8). As discussed above, the crystal fraction was determined from the decrease in the total signal intensity after 5 h.

The evolution of the distribution of the silicon atoms in the oligomers, nanoparticles, and silicalite crystals (from the undetected fraction of silicon atoms) during the crystallization of silicalite-1 is displayed in Figure 5. During the induction period (0–5 h), the silicon atoms were distributed among the oligomeric species and nanoparticles (i.e., 6.6± 0.2 and 93.4±4.0%, respectively). The crystal fraction obtained between 0 and 5 h was zero within the accuracy of the estimation from the NMR spectroscopy. Given the detection of all the silicon atoms and the presence of varying

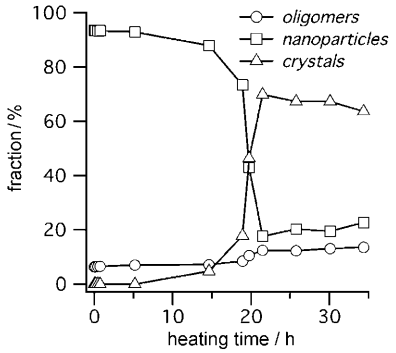

Figure 5. Fraction of oligomers, nanoparticles, and crystals determined from liquid-state ^{29}Si NMR spectra of samples quenched to room temperature after various heating times.

amounts of the 2-nm and 6-nm subpopulations of nanoparticles according to SAXS analysis, it is concluded that the broad NMR signals are due to both the 2- and 6-nm nanoparticles.

The crystal fraction became significant in the ^{29}Si NMR spectrum taken after heating for 15 h. The yield of crystals rose rapidly during the period of heating between 15 and 20 h (Figure 5). The crystal-yield curve derived from the silicon atoms undetected by NMR spectroscopic analysis agrees well with the development of Bragg reflections observed parallel to the SAXS analysis (Figure 3). It is revealed by NMR spectroscopic analysis that approximately 20% of the silicon atoms remain present in the nanoparticles in the final stage (heating for >20 h). Interestingly, over the entire crystallization process the fraction of oligomers remains relatively constant at around 10%. A slight increase in oligomers was noticed after a reaction time of around 20 h, which corresponds to the termination of the crystal-growth phase.

The evolution of the pH values is depicted in Figure 6. An increase in the pH value during zeolite crystallization is a well-known phenomenon.[31] The increase is attributed to the condensation reactions of SiOH/SiO$^-$ groups, thus giving rise to the formation of hydroxy anions. Apparently, the buffering capacity of the system is insufficient to keep the pH value constant. There were two increases in pH value:

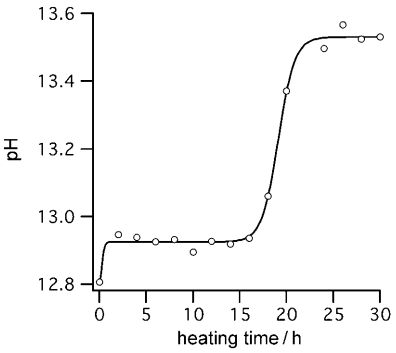

Figure 6. Evolution of the pH values at 22 °C of quenched samples. The black trace is a double sigmoid fit to the data.

the first occurred in the induction period (0–5 h) and proceeded in parallel with the formation of the 6-nm nanoparticles. During the period 5–15 h, which includes the nucleation and initial crystal-growth, the pH value remained constant. The period of extensive crystal growth (15–20 h) was characterized by a large increase in the pH value. This main jump in the pH value provoked a slight shift in the solubility equilibria of the system and slightly favored the fraction of silicon atoms in the oligomeric species (Figure 5).

The distribution of the Q^n environments in the oligomers against heating time is displayed in Figure 7. During the period that includes induction and the onset of crystal

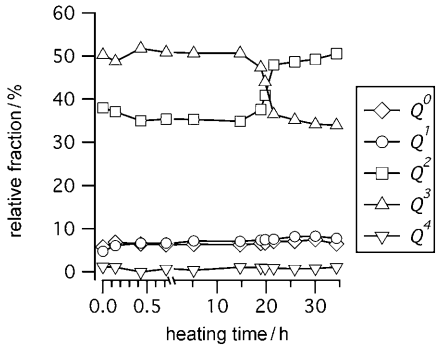

Figure 7. Q^n distribution of oligomers determined with liquid-state ^{29}Si NMR spectroscopy.

growth (0–15 h), the Q^n composition of the oligomers was quite constant. The monomer and end groups (i.e., Q^0 and Q^1, respectively) were present in insignificant amounts. The Q^2 and Q^3 silicon atoms were the main constituents of the oligomers. After the jump in pH value at around 18 h, the distribution of the Q^n environments in the oligomers changed. The Q^2 environments became more abundant than the Q^3 environments. The content of the Q^0, Q^1, and Q^4 silicon atoms remained low.

The evolution of silicate connectivity of nanoparticles is shown in Figure 8. The average silicate connectivity of nanoparticles (average n in Q^n) is shown in Figure 9. During the induction period (<5 h), the average connectivity of nanoparticles showed a significant increase (Figure 9), caused by a drop in the Q^3 environments and in favor of the Q^4 environments (Figure 8). The content of the Q^1 and Q^2 sites in nanoparticles remained essentially unchanged (Figure 8b).

The occurrence of condensation reactions in which Q^3 environments were converted into Q^4 environments was reflected in the evolution of the pH values, which showed a small but significant increase during the initial hours of the induction period (Figure 6). Such a change in connectivity can be taken as an indication of the aggregation of nanoparticles containing Q^3 environments. The restriction of condensation reactions to Q^3 environments is evident when the distribution of the Q^n environments in the nanoparticles in the totality of the silicon atoms is plotted against heating time (Figure 8b). Over the whole investigation, the Q^1 and Q^2 sites in the nanoparticles represented a constant share of

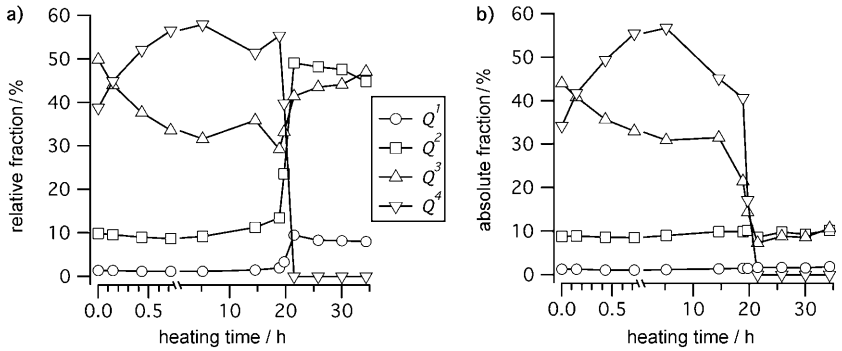

Figure 8. Q^n-type silicon atoms of nanoparticles determined with liquid-state ^{29}Si NMR spectroscopic analysis. a) Relative Q^n sites as a fraction of the silicon atoms in the nanoparticles; b) Q^n sites in nanoparticles as a fraction of the total silicon content of the synthesis sol.

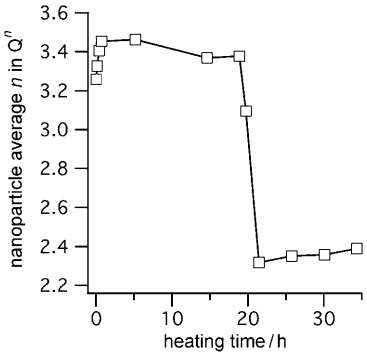

Figure 9. Average connectivity n of the Q^n-type silicon atoms in the nanoparticles.

the total silicon content of the sol of about 2 and 10%, respectively. The Q^1 and Q^2 environments were not involved in the condensation reactions in the induction period; furthermore, such sites were not involved in the crystal-growth phase either.

A major decrease in the concentration of the Q^3 and Q^4 sites in the nanoparticles was observed in the period of crystal growth at around 18 h (Figure 8b). Consequently, the average nanoparticle connectivity decreased (Figure 9). The residual nanoparticles present had low silicate connectivity, according to their Q^n distribution (Figure 8a), after the crystal-growth phase (>20 h). The persisting nanoparticles hardly contained any Q^4 environments. The Q^2 and Q^3 environments were present in about equal amounts, next to low amounts of the Q^1 silicon atoms. This Q^n distribution of the persisting nanoparticles is similar to the Q^n distribution in the oligomers (Figure 7). The residual nanoparticles seem to be composed of oligomers similar to those present in solution (compare the data points at heating times of >20 h; Figures 8a and 7).

Discussion

The combination of ^{29}Si NMR spectroscopic, DLS, and SAXS analysis leads to the following scenario in the silica speciation: The silicon atoms are present in four types of species: dissolved oligomers, nanoparticles that measure approximately 2 and 6 nm, and silicalite-1 crystals.

During the crystallization process of silicalite-1, the concentration of oligomers and their internal connectivity undergo little changes. Dissolved oligomers represent a constant 10% of all the silicon atoms. The most marked change is some depolymerization during the jump in pH value after heating for around 18 h, near the termination of the extensive crystal-growth period.

According to the SAXS analysis 2-nm nanoparticles are present during the whole crystallization process. The 2-nm nanoparticles are the only nanoparticles left in the final phase of the crystallization (>20 h). Therefore, the Q^n distribution in the nanoparticles observed in the final phase is that of the 2-nm nanoparticles (Figure 8a). Roughly, the 2-nm nanoparticles are composed of 45–50% of Q^2 and Q^3 sites, less than 10% of Q^1 sites, and no Q^4 sites. Out of the total amount of silicon atoms, the concentration of the Q^1 and Q^2 sites inside the nanoparticle fraction is invariant during the whole crystallization process (Figure 8b). The large content of Q^2 environments and the presence of Q^1 environments shows that these persistent 2-nm nanoparticles are little condensed. These nanoparticles may represent the loosely bound clusters of oligomers associated with TPA cations observed by Pelster et al. by using mass-spectrometric analysis.[32] The 2-nm nanoparticles represent approximately 20% of all the silicon atoms in the period after the growth of silicalite-1 crystals.

During the induction period (0–5 h), part of the initially present 2-nm nanoparticles grow to approximately 6 nm. In the case of an Ostwald-ripening-type growth mechanism, it is expected that 2-nm nanoparticles dissolve, while the 6-nm nanoparticles are formed. However, the SAXS data suggest that the size of the 2-nm nanoparticles is constant. This observation is consistent with an aggregative growth mechanism, but is in contradiction to an Ostwald ripening process. The nanoparticles grown to approximately 6 nm have a high content of Q^3 and Q^4 silicon atoms. The formation of 6-nm nanoparticles out of a fraction of 2-nm nanoparticles goes along with a gain in Q^4 environments at the expense of Q^3 environments. The selective conversion of Q^3 silicon environments into Q^4 sites suggests the occurrence of condensations reactions between particle-terminating silanols groups (i.e., Q^3). The fusion of particles results in a decrease in the surface/volume ratio. Within the first hour of the induction period, according to NMR spectroscopic analysis, the Q^3/Q^4 ratio dropped from 1.5:1 to 0.5:1. By assuming that the nanoparticles are spherical, the Q^4 environments are in the

core, and the Q^3 environments are in a 0.3-nm shell surrounding the core,[9] a change in the Q^3/Q^4 ratio from 1.5:1 to 0.5:1 would correspond to a size increase from 2.4 to 5 nm. By considering the nanoparticles to be stabilized by electrostatic interactions at the negatively charged silica surface, an additional layer of organic cations of 1 nm is expected because the ionic radius of a TPA cation is approximately 0.45 nm.[33] From the DLS experiments discussed above, the nanoparticles grew to such extent, that is, from 2.4 to 6 nm. This rough simulation suggests that the 6-nm particles have a fully condensed internal silicate network terminated with Q^3 silicon atoms. Such particles with a large number of covalent bonds are expected to have a long lifetime.

The induction period is the time needed to grow a fraction of the 2-nm subpopulation of nanoparticles to 6 nm. As discussed above, the remaining 2-nm particles are only slightly condensed and persist throughout the further crystallization reaction. The 6-nm particles, on the other hand, are consumed during the nucleation and growth of silicalite-1 according to SAXS analysis. A consequence of the decrease in the Q^3/Q^4 ratio during the formation of the 6-nm particles is the decrease in electrical-charge density. The Q^4 sites do not carry SiOH groups available for dissociation into SiO^-. During the nanoparticle aggregation from an average size of 2.4 nm to 6 nm, the maximal charge density, approximated as the number of Q^3 sites per particle, decreases about sevenfold. Consequently, the electrostatic repulsive potential is greatly decreased, thus leading to an enhanced aggregation probability. The condensation of the silicate network in the nanoparticles may thus trigger nucleation and aggregative growth. The induction period is the time needed to reach a critical concentration of condensed 6-nm nanoparticles. The first observed crystals measure some 20 nm (Figure 2). Bragg crystallinity was observed with SAXS analysis when the particle size reached about 50 nm (Figures 2 and 3).

Crystallization mechanism: Herein, previous reports of the crystallization of silicalite-1 models are confronted with the presently revealed evolution of silica speciation.

A first assumption is crystal growth from a monomer or dissolved oligomeric species. Given that only 10% of all silicon atoms are in a dissolved state (oligomers) and that the final crystal yield is 64%, such a solution-mediated mechanism necessarily would involve nanoparticle dissolution. Thermodynamically, the smallest of nanoparticles, that is, the 2-nm subpopulation, is the most sensitive to dissolution. However, according to both SAXS and NMR spectroscopic analysis, the 2-nm nanoparticles undergo little change in particle size and number.

A crystal-growth mechanism that involves the gradual dissolution of the ~6-nm nanoparticles also seems improbable because the Q^3/Q^4 ratio of dissolving nanoparticles is expected to increase, especially in the exponential growth stage at around 18 h, which was not observed (Figure 8a). The NMR spectroscopic data consistent with the SAXS analysis, show that the number rather than the size of the 6-nm particles decreases during crystal growth. The presence of nanoparticles of discrete sizes (i.e., 2 and 6 nm) is an argument against a mechanism that involves the gradual dissolution of nanoparticles to feed crystal growth. Growing crystals with sizes between 6 and 20 nm, if present at all, remained below the detection limits of DLS. Growth by monomer or oligomer addition in the size range 6–20 nm is unlikely. A mechanism that involves aggregation steps is more consistent with the presented results.

During the induction period, the nanoparticles undergo differentiation with respect to the structure and size of the silicate framework. To account for the observations, we postulate that the unheated system consists of two groups of nanoparticles. One group is too poorly polymerized to transform during heating into suitable building blocks for the crystallization, and one group that can aggregate to 6 nm with an increased degree of connectivity. By assuming that the insufficiently polymerized particles are formed upon mixing of the reagents and that these particles persist till the end, their Q^n distribution corresponds to the nanoparticle Q^n distribution observed after 20 h. In this hypothesis, the first nanoparticle population is rather insensitive towards increased temperatures on the crystallization timescale and remains small (ca. 2 nm) and poorly condensed. This small-size population of nanoparticles bears a resemblance to the oligomeric species, which also shows negligible changes upon heating. At the end of the induction period, the experimental data indicate that about 70% of the silicon atoms reside in 6-nm nanoparticles with a highly connected silica framework, 10% in dissolved oligomers, and 20% in poorly polymerized nanoparticles. The high concentration of 6-nm nanoparticles is consistent with the notion that silicalite-1 crystals nucleate and grow by direct addition of these particles, without involvement of oligomeric silicate species. Based on their high Q^4 content, we infer that the ~6-nm particles have zeolite-like connectivity. The connectivity and size of these particles remains constant during the major part of the growth stage. Mechanistically, the data are consistent with a growth mechanism through aggregation. The onset of aggregation into crystals may be related to the low electric charge density of the 6-nm building blocks, which eventually leads to colloidal destabilization.

On the basis of these arguments, a refined crystallization model is proposed (Figure 10). At the stage of preparing the clear sol, two groups of 2-nm particles are formed. A fraction of these nanoparticles contains merely aggregated oligomers, which do not contribute to the nucleation or growth processes and represent some 20% of the silicon atoms. The main part of the nanoparticles (70% of the total silicon atoms) has a suitable degree of internal condensation. These particles grow by aggregation to approximately 6 nm. A critical concentration of the 6-nm particles eventually is reached. Silicalite-1 nucleates and grows through the addition of these units. Although no direct evidence is provided, the 6-nm units presumably have a zeolitic character and oriented growth is presumed. Aggregative models presented in previous reports assume that the as-prepared nanoparticle

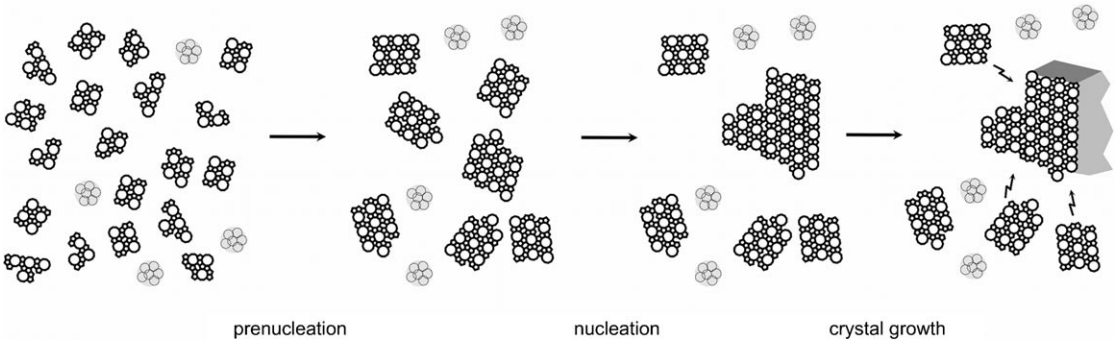

Figure 10. Scheme of the crystallization mechanism proposed herein. Particles with poorly developed framework connectivity are depicted in light gray; zones with zeolite-like framework connectivity are depicted in dark gray; the zigzag arrows indicate an aggregation event.

population is unstructured[3,17] (Figure 1a,b) or entirely MFI-structured[19,20] (Figure 1c). The silicate framework of initial nanoparticles in the model of Figure 10 is not uniform, but is either poorly or highly connected. This differentiation of nanoparticles already takes place during the synthesis of the clear sol at room temperature. Their framework connectivity determines their propensity for aggregation. During a prenucleation stage, the highly connected 2-nm nanoparticles selectively aggregate form to 6-nm nanoparticles. The framework connectivity of the 6-nm nanoparticles after prenucleation resembles the final zeolite and is invariable during a further course of crystallization. In terms of framework connectivity, the population of 6-nm nanoparticles is comparable to the nanoslabs or tablets of model c in Figure 1.

The aggregation of a fraction of nanoparticles with poorly developed topology during prenucleation, and subsequent transformation of the aggregate into a viable nucleus with zeolite framework connectivity (Figure 1a) was proposed by de Moor et al.[17] Whereas Davis et al. proposed that the formation of a nucleus takes place at the end of a chain of equilibria that connect nanoparticles with different degree of MFI framework structure (Figure 1b).[3] The nucleation event in the model presented herein is the aggregation of a fraction of Q^4 rich 6 nm nanoparticles.

It was proposed by de Moor et al. that crystal growth proceeds through the attachment of unstructured units to the surface of the nucleus and consequent development of the zeolite framework.[17] A quantitative model for growth through the aggregation of nanoparticles and subsequent framework rearrangement was developed by Nikolakis et al.[18] It was suggested by Davis et al. that growth occurs by the oriented attachment of intermediately structured nanoparticles to the nucleus.[3] It was also proposed that the attachment rates increase with the increasing degree of MFI structuring.[34] A common feature of models a and b in Figure 1 is that these show a well-defined nucleation event followed by growth by addition of individual nanoparticles. The initial system in model c only contains fully zeolitic nanoslabs followed by growth through consecutive oriented aggregation steps, that is, the nanoslabs couple sideways two by two to form tablets, which staple to intermediates that further cluster sideways to the crystals. This mechanism corresponds to the cluster–cluster aggregation of zeolite building blocks of increasing size. Similarly, Watson et al. proposed consecutive oriented aggregation that starts from cylindrical rather than slablike MFI-structured particles.[35]

In the model of Figure 10, growth starts by oriented aggregation of additional 6-nm nanoparticles with the nuclei. Attachment of individual 6-nm nanoparticles to the growing crystal is proposed rather than consecutive cluster–cluster aggregation steps (Figure 1c) because the 6-nm nanoparticles are observed throughout crystal growth and their size does not gradually increase during crystal growth.

The proposed model stresses the importance of the preparation of a clear sol at room temperature. The framework of nanoparticles already is determined to a large extent during the initial condensation reactions that take place after hydrolysis of TEOS in aqueous TPAOH. Only the fraction of nanoparticles with high connectivity in the starting clear sol is incorporated into the crystals. Methods to increase the amount of highly connected nanoparticles in the starting clear sol may therefore provide a pathway to increase the final yield of the crystal.

Conclusion

A refined model for the crystallization of silicalite-1 from a TEOS/TPAOH clear sol has been derived based on DLS, SAXS, pH, and ^{29}Si NMR experiments. The as-prepared clear sol contains oligomeric silicate species and two discrete populations of 2-nm nanoparticles with different framework connectivities. Oligomers and nanoparticles with low silicate framework connectivity do not participate in the crystallization. Nanoparticles with a highly connected silicate framework that resemble the final zeolite grow to approximately 6 nm during prenucleation. These 6-nm particles are the units for further nucleation and aggregative growth of colloidal silicalite-1 crystals.

Experimental Section

TEOS (Acros, 98%) was added to an aqueous solution of TPAOH in water (Alfa, 40 wt%) in a polypropylene vessel at room temperature with stirring. Water was added to the mixture after stirring for 20 min, thus resulting in a molar TEOS/TPAOH/H_2O composition of 25:9:400. This clear sol was aged for 24 h at room temperature before further manipulation or measurement.

DLS experiments: Analysis of a sample of an unheated clear sol at 25 °C and a sol heated at 95 °C for up to 12 h of reaction was performed on a CGS-3 apparatus from ALV (Langen, Germany) with a 22-mW HeNe (632.8 nm) laser. As the particle sizes are at the lower limit of the DLS technique, measurements were carried out at seven different scattering angles between 25 and 150°. The samples were filtered with 0.2-μm polytetrafluoroethylene (PTFE) membrane syringe filters (Alltech) and were introduced in glass tubes. The tubes were inserted after sealing into the preheated (25 or 95 ± 1 °C) measuring cell filled with *cis*-decaline as an index-matching fluid. The measurement time for each autocorrelation function was 60 s. DLS of the clear sol heated for between 10 and 32 h at 95 °C in a synthesis oven and subsequently quenched to room temperature under flowing water was performed with an ALV NIBS apparatus at 25 °C. These samples were diluted with water (100×) and filtered before measurement. At all times, the angular dependence of the scattered intensity was absent, which shows that the experiments were performed in the Rayleigh scattering regime. The measured autocorrelation functions (see Figure S1) were transformed to intensity-weighed relaxation-rate distributions, which was achieved by an inverse Laplace transformation least-squares fitting algorithm with maximal entropy regularization with NPK software.[23] The decay rates Γ, which correspond to the peak maxima, were determined by fitting Gauss curves to the peaks of the intensity-weighed decay-rate distributions. Diffusion coefficients D were calculated by linear fitting of the decay rates Γ at different scattering vectors Q according to the relationship $\Gamma = Dq^2$. A linear relation was found at all times, thus revealing diffusive processes. The viscosity of the reacting solution was determined in situ at 95 °C, using an AMVn rolling-ball viscosimeter (Anton Paar) calibrated with water at the measurement temperature. The viscosities of the unheated sol and the heated, quenched, and diluted samples were measured at 25 °C by using the same procedure. Hydrodynamic particle sizes were calculated from the diffusion coefficients and the corresponding viscosities with the Stokes–Einstein relation. Volume-weighed particle-size distributions were calculated with the ALV analysis software.

SAXS: Samples were prepared by reaction of a clear sol at 95 °C between 2 and 32 h and subsequent quenching to room temperature. The SAXS patterns of the unheated and heated sols were recorded at the ID02 high brilliance beamline (ESRF, Grenoble, France). The samples were loaded into 1.6-mm quartz capillaries. The X-ray wavelength was $\lambda = 9.95063$ 10^{-11} m. A FReLoN Kodak CCD mounted in a vacuum tube was used at a sample-to-detector distance of 0.8 m. Data treatment involved various detector corrections for flat-field response, spatial distortion, and dark current of the CCD, as well as normalization by the incident flux, sample transmission, sample path length, and exposure time. The resulting normalized two-dimensional images were averaged to obtain $I(q)$, which essentially refers to the differential scattering cross section $d\Sigma/d\Omega$ per unit length in $mm^{-1}sterad^{-1}$.

NMR spectroscopy: Samples for NMR spectroscopy were prepared by heating the initial clear sol at 95 °C and quenching to room temperature after 11 reaction times between 0 and 35 h. The ^{29}Si NMR spectroscopic experiments were carried out in 10-mm quartz tubes with a modified background-free commercial probe in a Bruker Avance 500 spectrometer at a resonance frequency of 99.353 MHz. The spectra of the heated sols were recorded with single-pulse acquisition at room temperature (24–25 °C) with a pulse of 8.5 μs (45°), a repetition delay time of 7 s, and 1024 accumulations. The spectra of the unheated sol were recorded with 12×1024 accumulations that started 5 min after adding water to the TEOS/TPAOH mixture. Under such conditions and on the basis of the Ernst angle equation, the measurements were quantitative for any resonance with a longitudinal relaxation time T_1 up to 20 s. Typical T_1 relaxation times in concentrated aqueous solution of silicate are below 17 s.[24] Longitudinal relaxation-time measurements in typical clear precursor sols of silicalite-1 have been investigated.[25] The T_1 values for silicate oligomers were within 8–18 s, whereas the T_1 values of the silicate species in the nanoparticles were one order of magnitude higher, that is, in the range 15–126 s. To overcome the effect of incomplete relaxation due to shorter repetition time, spectra of the unheated clear sol were recorded twice with repetition delay times of 7 and 92 s, which are long enough for full relaxation of all resonances with a pulse angle of 45°. This comparison allows determination of a correction factor for quantitative estimation of NMR spectra recorded when using a reduced recycle delay. Fitting of the spectra by following a procedure described previously[5,6] results in the quantification of three fractions: oligomers (narrow lines), nanoparticles (broad lines), and solid material (signal intensity loss). The silicon connectivity pattern of the two former fractions was therefore provided in terms of Q^n, where $n = 0$–4 represents the number of siloxane bonds of a silicon nucleus. Assignment of the Q^n environment was performed in accordance with previous work.[5,26–28]

pH values: The pH value of the sols was measured at 22 °C with a Mettler Toledo SevenMulti S40 equipped with an Inlab 418 electrode. Stable readouts of the pH values were obtained after 1 min.

Acknowledgements

We acknowledge the European Synchrotron Radiation Facility for provision of the synchrotron radiation facilities and we thank Anuj Shukla and Emanuela di Cola for assistance in using beamline ID02. We acknowledge Basavaraj Madivala, currently at the University of Delaware, Chemical Engineering, for assistance during the synchrotron X-ray measurements. A.A. is grateful to the Flemish FWO for a postdoctoral scholarship. L.R.A.F., C.E.A.K., and J.A.M. acknowledge financial support by ESA and the Belgian Prodex office. T.C. acknowledges the Flemish IWT for a Ph.D. scholarship. The work was supported by the Belgian government through the IAP-PAI network and by the Flemish government through long term structural funding to J.A.M. (Methusalem).

[1] A. E. Persson, B. J. Schoeman, J. Sterte, J. E. Otterstedt, *Zeolites* **1994**, *14*, 557–567.
[2] R. W. Corkery, B. W. Ninham, *Zeolites* **1997**, *18*, 379–386.
[3] T. M. Davis, T. O. Drews, H. Ramanan, C. He, J. Dong, H. Schnablegger, M. A. Katsoulakis, E. Kokkoli, A. V. Mccormick, R. L. Penn, M. Tsapatsis, *Nat. Mater.* **2006**, *5*, 400–408.
[4] D. Liang, L. R. A. Follens, A. Aerts, J. A. Martens, G. Van Tendeloo, C. E. A. Kirschhock, *J. Phys. Chem. C* **2007**, *111*, 14283–14285.
[5] A. Aerts, L. R. A. Follens, M. Haouas, T. P. Caremans, M.-A. Delsuc, B. Loppinet, J. Vermant, B. Goderis, F. Taulelle, J. A. Martens, C. E. A. Kirschhock, *Chem. Mater.* **2007**, *19*, 3448–3454.
[6] L. R. A. Follens, A. Aerts, M. Haouas, T. P. Caremans, B. Loppinet, B. J. Goderis, J. Vermant, F. Taulelle, J. A. Martens, C. E. A. Kirschhock, *Phys. Chem. Chem. Phys.* **2008**, *10*, 5574–5583.
[7] J. M. Fedeyko, J. D. Rimer, R. F. Lobo, D. G. Vlachos, *J. Phys. Chem. B* **2004**, *108*, 12271–12275.
[8] J. M. Fedeyko, D. G. Vlachos, R. F. Lobo, *Langmuir* **2005**, *21*, 5197–5206.
[9] J. L. Provis, J. D. Gehman, C. E. White, D. G. Vlachos, *J. Phys. Chem. C* **2008**, *112*, 14769–14775.
[10] S. Kumar, T. M. Davis, H. Ramanan, R. L. Penn, M. Tsapatsis, *J. Phys. Chem. B* **2007**, *111*, 3398–3403.
[11] S. Kumar, Z. P. Wang, R. L. Penn, M. Tsapatsis, *J. Am. Chem. Soc.* **2008**, *130*, 17284–17286.
[12] S. Mintova, N. Olson, J. Senker, T. Bein, *Angew. Chem.* **2002**, *114*, 2670–2673.
[13] C. S. Cundy, P. A. Cox, *Microporous Mesoporous Mater.* **2005**, *82*, 1–78.
[14] B. J. Schoeman, *Micropor. Mesopor. Mater.* **1998**, *22*, 9–22.

[15] S. L. Burkett, M. E. Davis, *Chem. Mater.* **1995**, *7*, 920–928.
[16] W. H. Dokter, H. F. van Garderen, T. P. M. Beelen, R. A. van Santen, W. Bras, *Angew. Chem.* **1995**, *107*, 122–125; *Angew. Chem. Int. Ed. Engl.* **1995**, *34*, 73–75.
[17] P. P. E. A. de Moor, T. P. M. Beelen, B. U. Komanschek, L. W. Beck, P. Wagner, M. E. Davis, R. A. van Santen, *Chem. Eur. J.* **1999**, *5*, 2083–2088.
[18] V. Nikolakis, E. Kokkoli, M. Tirrell, M. Tsapatsis, D. G. Vlachos, *Chem. Mater.* **2000**, *12*, 845–853.
[19] C. E. A. Kirschhock, R. Ravishankar, P. A. Jacobs, J. A. Martens, *J. Phys. Chem. B* **1999**, *103*, 11021–11027.
[20] C. E. A. Kirschhock, S. P. B. Kremer, J. Vermant, G. Van Tendeloo, P. A. Jacobs, J. A. Martens, *Chem. Eur. J.* **2005**, *11*, 4306–4313.
[21] A. Patis, V. Dracopoulos, V. J. Nikolakis, *J. Phys. Chem. C* **2007**, *111*, 17478–17484.
[22] J. D. Rimer, O. Trofymluk, A. Navrotsky, R. F. Lobo, D. G. Vlachos, *Chem. Mater.* **2007**, *19*, 4189- 4197.
[23] M. A. Delsuc, T. E. Malliavin, *Anal. Chem.* **1998**, *70*, 2146–2148.
[24] S. D. Kinrade, T. W. Swaddle, *J. Am. Chem. Soc.* **1986**, *108*, 7159–7162.
[25] M. Haouas, D. P. Petry, M. W. Anderson, F. Taulelle, *J. Phys. Chem. C* **2009**, *113*, 10838.
[26] M. Haouas, F. Taulelle, *J. Phys. Chem. B* **2006**, *110*, 3007–3014.
[27] V. Moravetski, J. R. Hill, U. Eichler, A. K. Cheetham, J. Sauer, *J. Am. Chem. Soc.* **1996**, *118*, 13015–13020.
[28] H. Cho, A. R. Felmy, R. Craciun, J. P. Keenum, N. Shah, D. A. Dixon, *J. Am. Chem. Soc.* **2006**, *128*, 2324–2335.
[29] S. Yang, A. Navrotsky, *Chem. Mater.* **2002**, *14*, 2803–2811.
[30] L. J. M. van de Ven, J. G. Post, J. H. C. van Hooff, J. W. de Haan, *J. Chem. Soc. Chem. Commun.* **1985**, 214–216.
[31] S. G. Fegan, B. M. Lowe, *J. Chem. Soc. Faraday Trans. 1* **1986**, *82*, 785–799.
[32] S. A. Pelster, W. Schrader, F. Schüth, *J. Am. Chem. Soc.* **2006**, *128*, 4310–4318.
[33] M. Jorge, S. M. Auerbach, P. A. Monson, *J. Am. Chem. Soc.* **2005**, *127*, 14388–14400.
[34] T. O. Drews, M. Tsapatsis, *Microporous Mesoporous Mater.* **2007**, *101*, 97–107.
[35] J. N. Watson, L. E. Iton, R. I. Keir, J. C. Thomas, T. L. Dowling, J. W. White, *J. Phys. Chem. B* **1997**, *101*, 10094–10104.

Received: June 19, 2009
Revised: November 13, 2009
Published online: January 13, 2010

